Inorganic Chemistry
Article
pubs.acs.org/IC

Selective Metal Exsolution in $BaFe_{2-y}M_y(PO_4)_2$ ($M = Co^{2+}, Ni^{2+}$) Solid Solutions

Ignacio Blazquez Alcover,[†] Sylvie Daviero-Minaud,[†] Rénald David,[‡,⊥] Dmitry Filimonov,[§] Marielle Huvé,[†] J. Paul Attfield,[∥] Houria Kabbour,[†] and Olivier Mentré*[,†]

[†]Université Lille Nord de France, UCCS, UMR-CNRS 8181, ENSCL-USTL, 59652 Villeneuve d'Ascq, France

[‡]Universite Picardié Jules Verne, Laboratoire de Réactivité et Chimie des Solides, UMR 7314, 33 rue Saint Leu,80039 Amiens Cedex, France

[§]Department of Chemistry, Moscow State University, 119991 Moscow, Russia

[∥]School of Chemistry and Centre for Science at Extreme Conditions, University of Edinburgh, Edinburgh EH9 3JZ, U.K.

Supporting Information

ABSTRACT: The 2D-Ising ferromagnetic phase $BaFe^{2+}{}_2(PO_4)_2$ shows exsolution of up to one-third of its iron content (giving $BaFe^{3+}{}_{1.33}(PO_4)_2$) under mild oxidation conditions, leading to nanosized Fe_2O_3 exsolved clusters. Here we have prepared $BaFe_{2-y}M_y(PO_4)_2$ ($M = Co^{2+}, Ni^{2+}$; $y = 0$, 0.5, 1, 1.5) solid solutions to investigate the feasibility and selectivity of metal exsolution in these mixed metallic systems. For all the compounds, after 600 °C thermal treatment in air, a complete oxidation of Fe^{2+} to Fe^{3+} leaves stable M^{2+} ions, as verified by ^{57}Fe Mössbauer spectroscopy, TGA, TEM, microprobe, and XANES. The size of the nanometric α-Fe_2O_3 clusters coating the main phase strongly depends on the y_M metal concentration. For M-rich phases the iron diffusion is hampered so that a significant fraction of superparamagnetic α-Fe_2O_3 particles (100% for $BaFe_{0.5-x}Co_{1.5}(PO_4)_2$) was detected even at 78 K. Although Ni^{2+} and Co^{2+} ions tend to block Fe diffusion, the crystal structure of $BaFe_{0.67}Co_1(PO_4)_2$ demonstrates a fully ordered rearrangement of Fe^{3+} and Co^{2+} ions after Fe exsolution. The magnetic behaviors of the Fe-depleted materials are mostly dominated by antiferromagnetic exchange, while Co^{2+}-rich compounds show metamagnetic transitions reminiscent of the $BaCo_2(PO_4)_2$ soft helicoidal magnet.

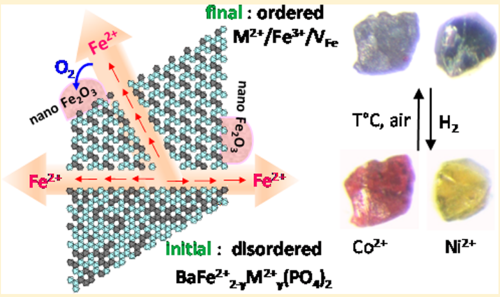

INTRODUCTION

In the rhombohedral $BaM_2(XO_4)_2$ compounds ($M = Co^{2+}, Ni^{2+}, Fe^{2+}$...; $X = V^{5+}, P^{5+}, As^{5+}$...), $M^{2+}O_6$ octahedra form a honeycomb lattice separated by $XO_4{}^{3-}$ oxo anions and have Ba^{2+}cations in their interlayer spaces. This leads to interlayer separations of approximately 8 Å that favor unusual quasi 2D magnetic behavior at low temperature, depending on the chemical nature of the M^{2+} ions. For instance, the cobaltite $BaCo_2(AsO_4)_2$ is a quasi-2D XY system in which the frustrated Co^{2+} magnetic moments are mainly confined in the basal planes responsible for magnetization steps below $T_N \approx 5.3$ K.[1] The same topology with Ni^{2+} ions in $BaNi_2(VO_4)_2$ leads to a quasi-2D antiferromagnet that orders below $T_N \approx 50$ K and undergoes a Kosterlitz−Thouless transition at $T_{KT} \approx 43$ K compatible with a weakly anisotropic 2D Heisenberg character.[2,3] For Fe^{2+} ions, the $BaFe_2(PO_4)_2$ phase was identified as a unique case of a 2D Ising ferromagnetic oxide with $T_C \approx 65$ K.[4] In this latter compound the oxidation process under mild conditions also proved to be fascinating.[5] Thanks to its 2D crystal structure, up to one-third of the initial Fe content can easily be removed by adapted medium-temperature treatments in air and reincorporated on heating under an H_2/Ar flow. In addition to the interest of preparing nanoclusters of α-Fe_2O_3 coating the crystals by this process, the diversity of full Fe/V_{Fe} ordering (where V_{Fe} denotes Fe vacancies) systematically identified for intermediate x values (x = 2/7, 1/3, 1/2, 2/3)[6,7] reflects an unprecedented easy in-plane diffusion of the Fe^{2+} ions. On the basis of the aforementioned observations, we decided to enlarge our study to the mild oxidation of mixed-metal $Ba(Fe,M)_2(PO_4)_2$ compounds. The preparation of pristine mixed Fe^{2+}/M^{2+} materials is challenging, due to the various synthetic routes required for specific M^{2+} ions and the complex phase diagrams. $BaNi_2(PO_4)_2$ can be prepared by a solid-state route,[8] but $BaCo_2(PO_4)_2$ is more complex due to a puzzling metamorphism with competition between at least six polymorphs.[9] These phases are stable under oxidizing conditions, but the stabilization of Fe^{2+} in $BaFe_2(PO_4)_2$ requires a hydrothermal route in reducing media (hydrazine solution), while so far our synthesis attempts by solid-state routes led to other forms, beyond the scope of this paper. In this paper we report $BaFe_{2-y}M_y(PO_4)_2$ solid solutions (M = Co, Ni) prepared under hydrothermal conditions and we discuss the metal exsolution and its reversibility in comparison to the behavior of the parent $BaFe_2(PO_4)_2$ phase.

Received: June 19, 2015
Published: August 19, 2015

DOI: 10.1021/acs.inorgchem.5b01360
Inorg. Chem. 2015, 54, 8733−8743

Table 1. Expected and Experimental Compositions, Refined Unit Cell Parameters, and Detected Impurities for Synthesized Solid Solutions of $BaFe_{2-y}M_y(PO_4)_2$ (As Prepared)[a]

as prepared				after exsolution 12 h, 600 °C							
								paramagnetism			
								μ_{eff}			
expected composition % Fe/M	microprobe composition % Fe/M	*a*, *c* (Å)	impurity	expected composition % Fe/M	microprobe composition % Fe/M	*a*, *c* (Å)	MB (78 K) % Fe^{3+}_{phase}/ % $Fe^{3+}_{Fe_2O_3}$	calcd	exptl	θ_{cw}	subproduct phase
$BaFe_2(PO_4)_2$ 100	$BaFe_2$ 100	4.87(3), 23.36(8)		$BaFe_{1.33}(PO_4)_2$ 100	$BaFe_{1.34}$ 100	4.74(7), 23.72(5)	64/36	6.82	7.01	−35.7	Fe_2O_3
$BaFe_{1.5}Co_{0.5}(PO_4)_2$ 75	$BaFe_{1.54}Co_{0.46}$ 77	4.86(8), 23.33(4)		$BaFe_{1.03}Co_{0.46}(PO_4)_2$ 67	$BaFe_{1.44}Co_{0.40}$ 78	4.78(3), 23.66(2)	67/33	6.55	7.74	−11.4	Fe_2O_3
$BaFeCo(PO_4)_2$ 50	$BaFe_{0.98}Co_{1.02}$ 49	4.86(3), 23.29(5)		$BaFe_{0.65}Co_{1.02}(PO_4)_2$ 40	$BaFe_{0.85}Co_{1.00}$ 46	4.81(6), 23.59(5)	68/32	6.17	7.16	33.7	Fe_2O_3
$BaFe_{0.5}Co_{1.5}(PO_4)_2$ 25	$BaFe_{0.68}Co_{1.32}$ 34	4.85(7), 23.261		$BaFe_{0.45}Co_{1.32}(PO_4)_2$ 18	$BaFe_{0.55}Co_{1.45}$ 27	4.83(3), 23.38(0)	75/25	5.96	7.49	41.0	
$BaFe_{1.5}Ni_{0.5}(PO_4)_2$ 75	$BaFe_{1.54}Ni_{0.46}$ 77	4.85(8), 23.36(6)		$BaFe_{1.03}Ni_{0.46}(PO_4)_2$ 67	$BaFe_{1.21}Ni_{0.46}$ 72	4.78(8), 23.55(6)	64/36	6.30	5.72	−24.4	Fe_2O_3
$BaFeNi(PO_4)_2$ 50	$BaFe_{1.06}Ni_{0.94}$ 53	4.83(6), 23.35(6)	$BaHPO_4$	$BaFe_{0.71}Ni_{0.94}(PO_4)_2$ 40	$BaFe_{0.83}Ni_{0.85}$ 49	4.78(9), 23.46(9)	73/27	5.69	7.58	−59.6	Fe_2O_3
$BaFe_{0.5}Ni_{1.5}(PO_4)_2$ 25	$BaFe_{0.55}Ni_{1.45}$ 28	4.81(5), 23.33(9)	$BaHPO_4$	$BaFe_{0.37}Ni_{1.45}(PO_4)_2$ 18	$BaFe_{0.37}Ni_{1.22}$ 23	4.79(4), 23.39(3)	66/34	4.95	5.7	−24.3	$Ba_2P_2O_7$

[a] Expected composition and expected paramagnetic moments μ_{eff}, experimental compositions, unit cell parameters, ratios $Fe^{3+}_{phase}/Fe^{3+}_{Fe_2O_3}$, magnetic parameters, and subproduct phases for exsolved phases (after exsolution at 12 h and 600 °C) are also shown.

EXPERIMENTAL SECTION

$BaFe_{2-y}M_y(PO_4)_2$ phases have been prepared for M = Co, Ni and y_{Co}, y_{Ni} = 0.5, 1, 1.5. $CoCl_2\cdot 6H_2O$ (Alfa Aesar, 99.90%), $NiCl_2\cdot 6H_2O$ (Alfa Aesar, 98.00%), $FeCl_2\cdot 4H_2O$ (Aldrich, 98.00%), $BaCO_3$ (Aldrich, 99.00%), H_3PO_4 (Prolabo, 85.00%), and hydrazine monohydrate ($N_2H_4\cdot H_2O$, Alfa Aesar, 98.00%) were used as reactants as received. The hydrazine, although systematically in excess, was added in a proportion related to the iron content (1.2−0.75 mL for 25 mL of water) and serves as a reducing agent to stabilize Fe^{2+} in the solution. The phases were synthesized by using stoichiometric mixtures of metal chlorides (~1.5 g of metal precursor for 25 mL of water) and a microwave-assisted solvothermal method with heating at 220 °C, as described previously for the pristine $BaFe_2(PO_4)_2$.[5] The title materials were always obtained as the main phase with a variable amount of polycrystalline $BaHPO_4$. This impurity can be separated and removed after sonication in ethanol. To observe the metal exsolution, all samples were heated in air at 600 °C for 12 h and were oven-cooled to room temperature. As-prepared and reheated phases were characterized by several techniques.

The accurate composition was determined by microprobe analysis. A Cameca SX100 electron probe microanalyzer (EPMA) was used to perform elemental analysis. Quantifications of Fe, Co, Ni, Ba, and P were carried out at 20 kV and 20 nA with a spot size of 20 μm. A LiF crystal was used to detect the Fe, Co, and Ni Kα X-rays and a PET crystal to detect the P Kα and Ba Lα X-rays. Oxygen was calculated by difference to 100 wt % and taken into account for matrix corrections. Standards used for quantification were made of pure Fe_2O_3, Co, Ni, apatite ($Ca_5(PO_4)_3(OH)$), and $BaSO_4$ powder pressed into small plates. Means and standard deviations were calculated from measurements carried out at least 10 different places on each sample.

Transmission electron microscopy studies and EDX analysis were performed on a FEI Tecnai G2 20 microscope. The material was crushed and dropped in the form of aqueous or alcohol suspensions on carbon-supported copper grids followed by evaporation under ambient conditions.

Powder X-ray diffraction (PXRD) was performed using a Bruker D8 Advance diffractometer, with a Brag Brentano geometry and monochromated Cu Kα radiation. The lattice parameters have been refined by profile matching using FULLPROF.[10]

The thermogravimetric analyses (TGA) were carried out with a Shimatzu DTG-60 M instrument from room temperature to 700 °C in air at a 5 °C/min heating rate.

The exsoluted phases were also characterized by ^{57}Fe Mossbauer spectroscopy in order to verify the Fe valence. ^{57}Fe Mössbauer spectroscopy was performed in a transmission mode using a constant-acceleration spectrometer (MS1104, Rostov-na-Donu, Rossia) coupled with a nitrogen cryostat. A ^{57}Co/Rh γ-ray source, maintained at room temperature, was used for the measurements. The spectrometers were calibrated with standard α-Fe or sodium nitroprusside absorbers. All isomer shift values (IS) are referenced to α-Fe. The spectral evaluation was carried out using "UnivemMS" and custom least-squares fitting software.

Single-crystal diffraction of the exsolved $BaFe_{2/3}Co(PO_4)_2$ phase was collected using a Duo Bruker Kappa APEX 2 diffractometer with Mo Kα radiation (λ = 0.7107 Å, graphite monochromator) equipped with a CCD (coupled charge device) detector. The ω-scan angle was fixed to 0.5°, and the D_x parameter was fixed at 35 mm. Diffraction intensities were extracted and corrected for Lorentz and Polarization using the Bruker program Saint Plus 6.02.[11] The unit-cell parameters were refined from the full data set. Multiscan absorption correction was performed using SADABS.[12] The crystal structure was determined by the charge-flipping method using the Superflip program,[13] and the Jana 2006 program was used for structure refinement.[14]

X-ray absorption near edge spectroscopy (XANES) was performed at the DIFFABS beamline of the SOLEIL synchrotron facility. The aim of the XANES experiment was to compare the initial and final valences of Co and Ni. The samples were prepared by deposition of well-ground powder sieved at 10 μm, and all measurements were performed in reflection mode at room temperature in air. Cobalt and nickel samples, before and after the thermal treatment, were measured around cobalt (7.65−7.90 keV), nickel (8.25−8.50 keV), and iron (7.05−7.30 keV) K-edges, respectively, with a four-element SDD silicon drift detector for X-ray fluorescence measurement.

For magnetic characterization, magnetization cycles at 2 and 300 K and temperature-dependent magnetic susceptibility were measured on a MPMS SQUID magnetometer (Quantum Design). Measurements were performed using zero field cooling (ZFC) and field cooling (FC) procedures under a 0.1 T field.

RESULTS AND DISCUSSION

Fe/M Compositions. $BaFe_{2-y}M_y(PO_4)_2$ (M = Co, Ni) samples have been prepared using stoichiometries corresponding to y_M = 0, 0.5, 1.0, 1.5. Apart from minor secondary phases such as $BaHPO_4$, PXRD patterns show single phases with

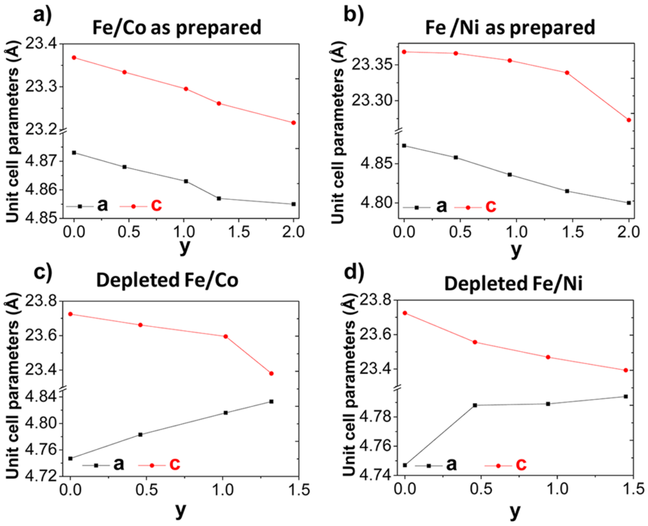

Figure 1. Rhombohedral unit cell parameters as a function of y for (a) as-prepared $BaFe_{2-y}Co_y(PO_4)_2$, (b) as-prepared $BaFe_{2-y}Ni_y(PO_4)_2$, (c) depleted $BaFe_{2-y}Co_y(PO_4)_2$, and (d) depleted $BaFe_{2-y}Ni_y(PO_4)_2$.

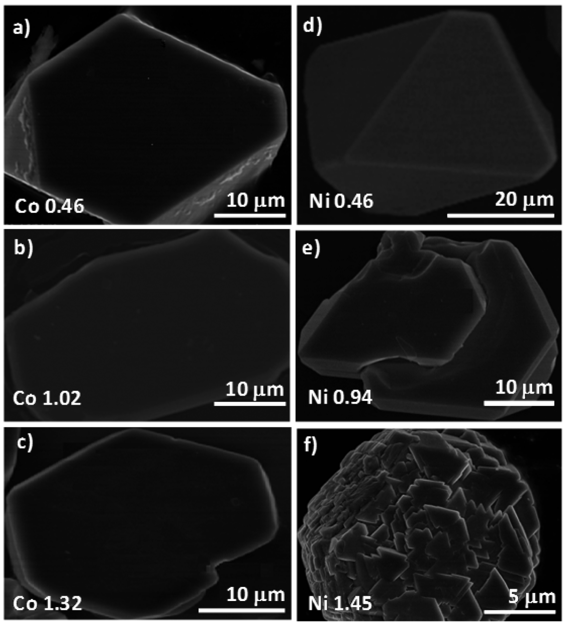

Figure 2. SEM images of $BaFe_{2-y}M_y(PO_4)_2$ (a−c) for M = Ni^{2+} and (d−f) for M = Co^{2+} with evidence of size reduction along the Ni series.

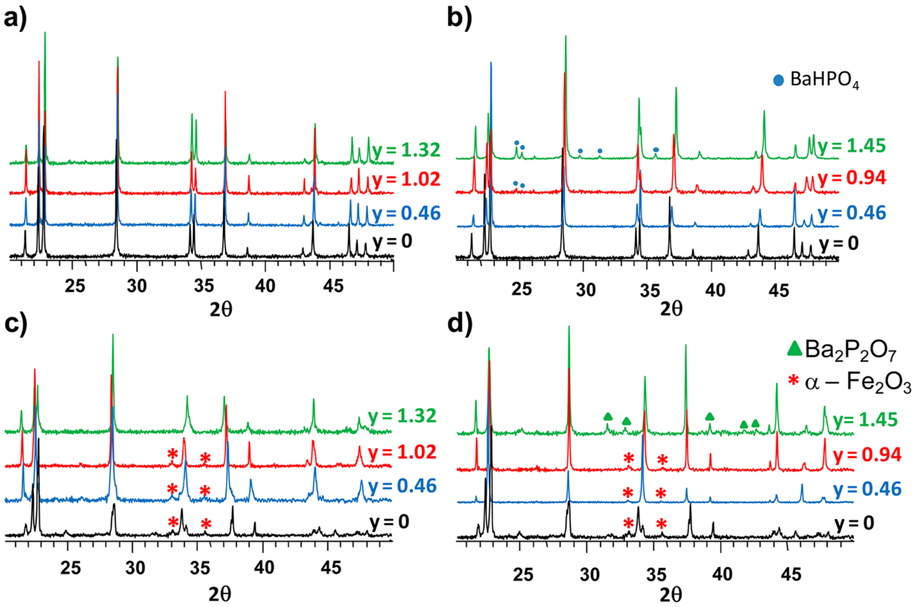

Figure 3. Powder XRD patterns for $BaFe_{2-y}Co_y(PO_4)O_2$ as prepared (a) and after thermal treatment (c) and for $BaFe_{2-y}Ni_y(PO_4)O_2$ as prepared (b) and after thermal treatment (d).

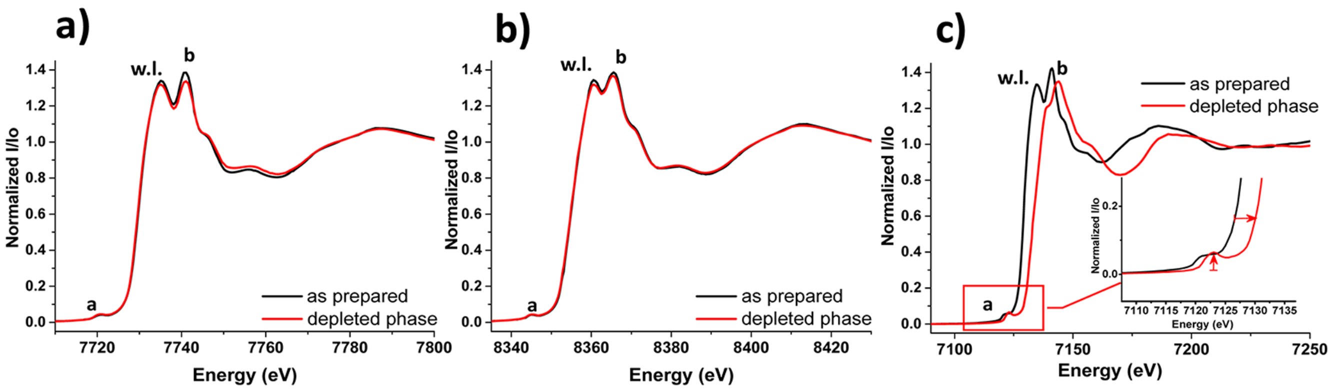

Figure 4. Comparison between the XANES spectra of as-prepared compounds and Fe depleted phase after thermal treatment for (a) $BaFe_{0.58}Co_{1.32}(PO_4)_2$ at the Co K edge, (b) $BaFe_{0.55}Ni_{1.45}(PO_4)_2$ at the Ni K edge, and (c) $BaFe_{0.58}Co_{1.32}(PO_4)_2$ at the Fe K edge.

homogeneous M/Fe compositions. However, microprobe analyses on pressed pellets show that the Fe/M incorporation during the hydrothermal treatment is not fully stoichiometric, after averaging around 10 points with a very small dispersion. Results are given in Table 1. For M = Ni the Fe/(Fe + M) ratio reflects the experimental stoichiometries in the full range with only slight deviations. For M = Co, we note that the stoichiometry is followed until y_{Co}= 1, while for the Co-rich sample (y_{Co} = 1.5) the composition deviates significantly from the ideal one, as we find Fe/(Fe + M) = 34% rather than 25%. This result is reproducible after examination of two different samples prepared with the same starting ratio and indicates different reactivities of Fe^{2+} versus Co^{2+} ions under our experimental conditions while Fe^{2+} and Ni^{2+} retain similar reactivities.

In view of the high accuracy on transition-metal contents by microprobe analysis, we will use these values as experimental "y_M" compositions. For Ba analysis, the deviation from the expected Ba/M ratio is not more than 5% (e.g., expected value 1/2, experimental value 1.11/2 for $BaFe_{0.55}Ni_{1.45}(PO_4)_2$). The PXRD patterns show that as-prepared $BaFe_{2-y}M_y(PO_4)_2$ (M = Co, Ni) samples crystallize with the same rhombohedral lattice as the parent $BaM_2(XO_4)_2$ phases. The evolution of the lattice parameters versus y_M is plotted in Figure 1a,b for the M = Co, Ni systems, respectively. Both the *a* and *c* parameters decrease versus y_M, following the differences in ionic radii ($r(Fe^{2+})$ = 0.78 Å < $r(Co^{2+})$ = 0.745 Å < $r(Ni^{2+})$ = 0.69 Å).[15]

Microstructure. After hydrothermal synthesis, the $BaHPO_4$ second phase, mentioned in the Experimental Section, can largely be removed by sonication in ethanol and evacuation of the upper colloid. The degree of separation between the two phases depends on the crystal size of $Ba(Fe,M)_2(PO_4)_2$ in comparison to submicron $BaHPO_4$ grains. Representative SEM images of as-prepared $Ba(Fe,M)_2(PO_4)_2$ particles are shown in Figure 2. For the Co series (Figure 2a−c), the typical crystal size of ∼40 μm is rather independent of the y_{Co} ratio. However, in the Fe/Ni case (Figure 2d,e), the situation is very different. The crystal size decreases drastically with the y_{Ni} ratio from ∼40 μm (y = 0.46) to ∼5 μm (y = 1.45) within agglomerate clusters. These features have dramatic effects on the efficiency of removal of $BaHPO_4$, whose contribution can be observed on PXRD patterns for y_{Ni} = 0.94, 1.45. Apart from $BaHPO_4$, no extra peak was detected by PXRD of the as-prepared samples (see Figure 3a,b) or by electron diffraction, which suggest a

DOI: 10.1021/acs.inorgchem.5b01360
Inorg. Chem. 2015, 54, 8733−8743

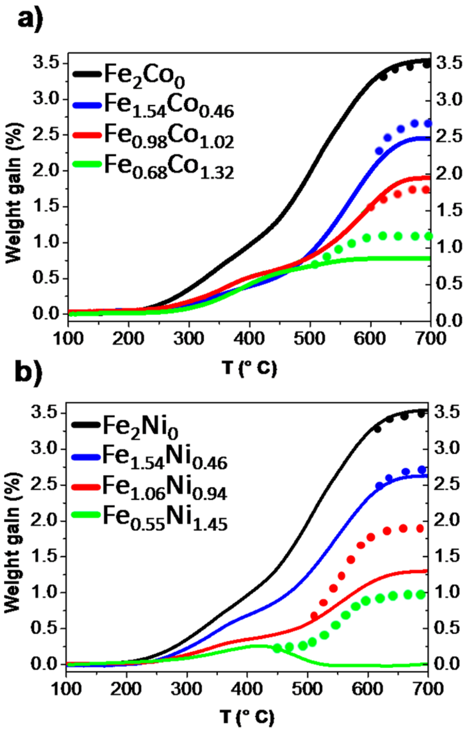

Figure 5. Thermogravimetric analysis (TGA) for (a) $BaFe_{2-y}Co_y(PO_4)_2$ and (b) $BaFe_{2-y}Ni_y(PO_4)_2$. Experimental curves are shown by full lines, and dotted lines give ideal weight gain on the basis of the microprobe formula according to the Fe-only exsolution (eq 1).

statistical Fe/M occupancy in the cation sites without superstructure formation.

After $BaFe_{2-y}M_y(PO_4)_2$ (M = Co, Ni) compounds were heated at 600 °C for 12 h, we observed significant changes of the PXRD patterns as shown in Figure 3c,d. From our prior experience on the exsolved $BaFe_{2-x}(PO_4)_2$ phases leading to a variety of triclinic Fe-deficient crystal structures, we expected small triclinic splittings of the main reflections while weak supercell spots are expected due to Fe/V_{Fe} order.[6] However, laboratory Cu Kα PXRD patterns of exsolved Fe/M samples were satisfactorily indexed by the parent rhombohedral unit cells, although peak broadening was sometimes observed at high 2θ and attempted determination of more accurate lattice parameters using synchrotron data was hampered by minor variations in the deficiency parameter x leading to the copresence of several polytypes. The refined lattice parameters and the corresponding Fe/M microprobe analyses are given in Table 1. In the full y_M range for M = Co, Ni, there is a significant contraction of the a parameter together with a c dilatation in comparison to the values for as-prepared compounds (see Figure 1c,d for Co and Ni, respectively). As shown for the pure Fe compound ($y = 0$), this evolution shows the creation and distribution of vacancies in the original honeycomb layers. The increase of the interlayer spacing, measured from c, is due to the stacking between non fully planar M-depleted layers, similar to the c increase from $BaFe_2(PO_4)_2$ to $BaFe_{2-x}(PO_4)_2$ compounds (at $y = 0$).[7] For our $y > 0$ materials, symmetry lowering was not verified using laboratory PXRD data and the absence of superstructure peaks suggests the formation of disordered rhombohedral phases in contrast to the triclinic supercells in $BaFe_{2-x}(PO_4)_2$ phases. However, this statistical rhombohedral model is partially refuted by single-crystal XRD data, as discussed later. It is noteworthy that the Fe-rich phases show more dramatic changes of their lattice parameters after exsolution in comparison to Co/Ni-rich phases, giving initial evidence for the preferred exsolution of Fe^{2+} ions.

Although not fully understood, it is clear that Fe-exsolution processes in Fe^{2+}/oxo anion systems such as $BaFe_2(PO_4)_2$, the olivine Fe_2SiO_4,[16] and $LiFe(PO_4)$,[17] are driven by the Fe^{2+}/Fe^{3+} redox properties. An indirect measure of the relative cationic stability in these systems is given during the charge/discharge cycling of $LiM(PO_4)$ cathodes by the Mn^{3+}/Mn^{2+} (4.1 V), Co^{3+}/Co^{2+} (4.8 V), and Ni^{3+}/Ni^{2+} (5.4 V) couples, which show increasing redox potentials that are all higher than that of the Fe^{3+}/Fe^{2+} couple (3.5 V).[18] Furthermore, the exsolution of only Fe^{2+} from mixed-metal $Li(Fe,Mn)_{1-x}PO_4$ phases was recently demonstrated, leaving stable Mn^{2+} but with complete oxidation of Fe^{2+} into Fe^{3+} and the formation of outer Fe_2O_3 grains.[19] In our mixed-metal compounds, the ideal full Fe oxidation reaction can be written

$$\begin{aligned} &BaFe^{2+}{}_{2-y}M^{2+}{}_y(PO_4)_2 + (2-y)/4O_2 \\ &\quad \rightarrow BaFe^{3+}{}_{(4-2y)/3}M^{2+}{}_y(PO_4)_2 + [(2-y)/6]Fe^{3+}{}_2O_3 \end{aligned} \tag{1}$$

After exsolution, the ideal expected ratio $Fe^{3+}{}_{phase}/Fe^{3+}{}_{hematite}$ between the depleted phase and the external Fe_2O_3 cluster is 2. Shifts from this value may evidence incomplete oxidation or other competing reactions such as partial or full removal of the M^{2+} cocation. The hypothetical chemical reaction for full M^{2+} removal is given by the following reactions in the Ni and Co cases, respectively, taking into account the stability of NiO in our experimental conditions. In the case of cobalt, the thermodynamic stability of Co_3O_4 (i.e., $CoO_{1.33}$) in comparison to that of CoO up to ~900 °C was considered:

$$\begin{aligned} &BaFe^{2+}{}_{2-y}Ni^{2+}{}_y(PO_4)_2 + [(2-y)/4]O_2 \\ &\quad \rightarrow BaFe^{3+}{}_{2-y}Ni^{2+}{}_{(3y-2)/2}(PO_4)_2 + [(2-y)/2]NiO \end{aligned} \tag{2_{Ni}}$$

$$\begin{aligned} &BaFe^{2+}{}_{2-y}Co^{2+}{}_y(PO_4)_2 + [(2.66-1.33y)/4]O_2 \\ &\quad \rightarrow BaFe^{3+}{}_{2-y}Co^{2+}{}_{(3y-2)/2}(PO_4)_2 + [(2-y)/2]CoO_{1.33} \end{aligned} \tag{2_{Co}}$$

We note that eqs 1 and 2Ni are not discriminating in terms of oxygen mass uptake, which is $[(2-y)/4]O_2$ in both cases.

Metal Oxidation States before and after Exsolution by XANES. $BaFe_{\sim0.5}M_{\sim1.5}(PO_4)_2$ samples were studied as prepared and after heating in order to compare their spectral evolution before and after the extrusion process. All measurements have been performed using powders in air at room temperature.

The edge energies for Ni^{2+} and Co^{2+}, marked by the white line (w.l.) and those of the pre-edge features (a) shown in Figure 4a,b, are not modified after heat treatment; hence, the extrusion process does not affect the cobalt or nickel redox, at the experimental resolution.

At the iron K edge, the evolution of XANES spectra clearly shows an edge shift (w.l.) and pre-edge evolution (a) related to the $Fe^{2+} \rightarrow Fe^{3+}$ oxidation process. This is shown in Figure 4c for the Co-rich phase. The same behavior has been observed for the exsolved Ni-rich phase. We therefore conclude that the redox changes induced by the extrusion process in the M-

DOI: 10.1021/acs.inorgchem.5b01360
Inorg. Chem. 2015, 54, 8733−8743

Table 2. ^{57}Fe Mössbauer Hyperfine Parameters of the Oxidized $BaFe_{1-y}M_y(PO_4)_2$ Compounds[a]

T, K	ideal composition	component	IS, mm/s ± 0.01	ΔE_Q, mm/s ± 0.01	H_{Hf}, T ± 0.1	*A* % ± 1	*G*, mm/s ± 0.01	assignment
300	$BaFe_{1.33}(PO_4)_2$	F2S1	0.37	−0.14	51.8	38	0.34	Fe_2O_3
		F2D2	0.40	1.19		31	0.28	Fe^{3+} (1)
		F2D3	0.42	0.81		31	0.27	Fe^{3+} (2)
78	$BaFe_{1.33}(PO_4)_2$	F2S2	0.49	0.02	53.7	12	0.30	Fe_2O_3(i-im)
		F2S2	0.49	0.32	54.0	24	0.28	Fe_2O_3(ii-m)
		F2D4	0.52	1.18		32	0.26	Fe^{3+} (1)
		F2D5	0.54	0.81		32	0.26	Fe^{3+} (2)
300	$BaFe_{1.03}Co_{0.46}(PO_4)_2$	C05S1	0.35	−0.19	51.7	35	0.32	Fe_2O_3
		C05D1	0.39	1.13		27	0.30	Fe^{3+} (1)
		C05D2	0.40	0.76		38	0.30	Fe^{3+} (2)
78	$BaFe_{1.03}Co_{0.46}(PO_4)_2$	C05S2	0.48	−0.20	53.5	19	0.28	Fe_2O_3(i-nm)
		C05S3	0.50	0.07	53.8	14	0.28	Fe_2O_3(ii-im)
		C05D3	0.54	1.11		29	0.29	Fe^{3+} (1)
		C05D4	0.54	0.76		38	0.28	Fe^{3+} (2)
300	$BaFe_{0.65}Co_{1.02}(PO_4)_2$	C1S1	0.37	−0.18	51.6	34	0.29	Fe_2O_3
		C1D1	0.43	0.93		66	0.33	Fe^{3+} (1)
78	$BaFe_{0.65}Co_{1.02}(PO_4)_2$	C1S2	0.49	−0.03	53.3	16	0.33	Fe_2O_3(i-nm)
		C1S3	0.49	0.18	54.4	19	0.29	Fe_2O_3(ii-m)
		C1D2	0.55	0.93		66	0.34	Fe^{3+} (1)
300	$BaFe_{0.45}Co_{1.32}(PO_4)_2$	C15S1	0.37	−0.21	51.5	28	0.33	Fe_2O_3
		C15D1	0.43	0.93		72	0.34	Fe^{3+} (1)
78	$BaFe_{0.45}Co_{1.32}(PO_4)_2$	C15S2	0.49	−0.20	53.2	25	0.29	Fe_2O_3(i-nm)
		C15D2	0.54	0.93		75	0.32	Fe^{3+} (1)
300	$BaFe_{1.03}Ni_{0.46}(PO_4)_2$	N05S1	0.38	−0.12	52.0	38	0.37	Fe_2O_3
		N05D1	0.42	1.10		30	0.25	Fe^{3+} (1)
		N05D2	0.43	0.74		32	0.25	Fe^{3+} (2)
78	$BaFe_{1.03}Ni_{0.46}(PO_4)_2$	N05S2	0.47	0.03	53.5	10	0.27	Fe_2O_3(i-im)
		N05S3	0.48	0.28	53.9	25	0.29	Fe_2O_3(ii-m)
		N05D3	0.53	1.08		31	0.27	Fe^{3+} (1)
		N05D4	0.53	0.76		34	0.27	Fe^{3+} (2)
300	$BaFe_{0.71}Ni_{0.94}(PO_4)_2$	N1S1	0.34	−0.09	52.0	30	0.40	Fe_2O_3
		N1D1	0.38	1.09		37	0.31	Fe^{3+} (1)
		N1D2	0.40	0.76		33	0.29	Fe^{3+} (2)
78	$BaFe_{0.71}Ni_{0.94}(PO_4)_2$	N1S2	0.48	0.21	54.1	21	0.30	Fe_2O_3(i-m)
		N1S3	0.51	0.33	54.8	7	0.27	Fe_2O_3(ii-m)
		N1D3	0.53	1.09		38	0.29	Fe^{3+} (1)
		N1D4	0.54	0.76		34	0.27	Fe^{3+} (2)
300	$BaFe_{0.37}Ni_{1.45}(PO_4)_2$	N15D1	*(0.34)*	0.91		*(33)f*	0.46	*SP(Fe_2O_3)*
		N15D2	0.44	1.07		35	0.29	Fe^{3+} (1)
		N15D3	0.45	0.71		32	0.29	Fe^{3+} (2)
78	$BaFe_{0.37}Ni_{1.45}(PO_4)_2$	N15D4	*(0.47)*	0.95		*(33)f*	0.43	*SP(Fe_2O_3)*
		N15D5	0.55	1.02		33	0.29	Fe^{3+} (1)
		N15D6	0.55	0.75		34	0.29	Fe^{3+} (2)

[a] Definitions: IS, isomer shift relative to α-Fe at ambient temperature; ΔE_Q, apparent quadrupole shift; H_{Hf}, magnetic hyperfine field; *G*, line width; *A*, relative spectral area.

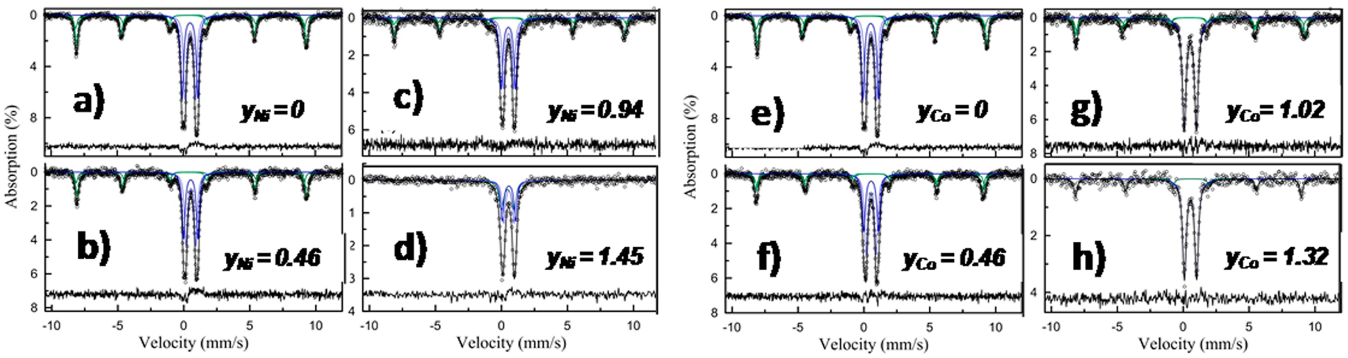

Figure 6. Mössbauer spectra at 78 K of depleted $BaFe_{2-y}Ni_y(PO_4)_2$ (a−d) and $BaFe_{2-y}Co_y(PO_4)_2$ (e−h).

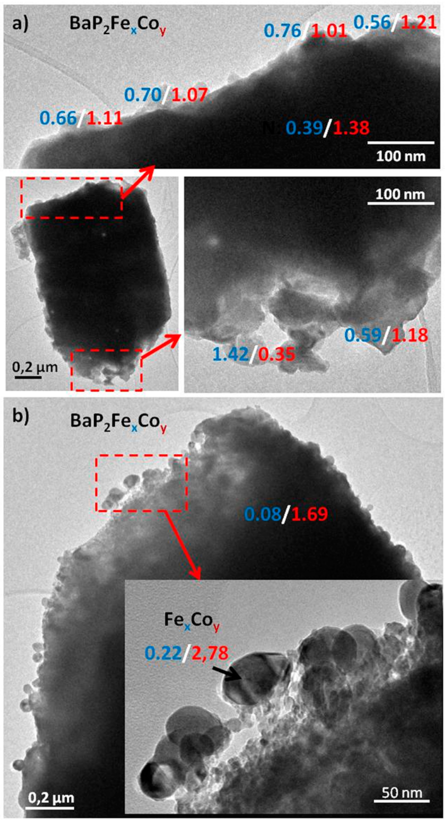

Figure 7. Coupled TEM images and EDX analysis for two different crystals (a) and (b) of $BaFe_{0.45}Co_{1.32}(PO_4)_2$. The Fe/Co ratio (indicated respectively in blue and red) shows the homogeneous expected composition core and Fe surfacial enrichment due to intergrown Fe_2O_3 (a) and cobalt excess in the core with Fe-doped cobalt oxide at the surface (b).

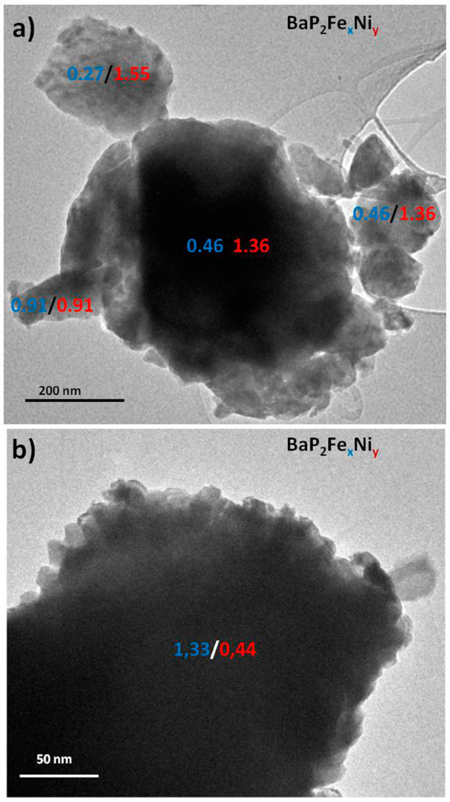

Figure 8. Coupled TEM images and EDX analysis of (a) $BaFe_{0.37}Ni_{1.45}(PO_4)_2$ with chemical changes at the surface and (b) $BaFe_{1.03}Ni_{0.46}(PO_4)_2$ with homogeneous but different composition from EDX.

substituted compounds only concern the iron atoms, at the limit of the experimental resolution.

The TGA mass uptakes (ΔM) have been correlated with Mössbauer spectroscopy results. The TGA plots versus "y_M" are compared to ideal ΔM_{calcd} values calculated using eq 1 for both the Fe/Co and Fe/Ni systems (see Figure 5). Apart from iron-poor compositions, all compounds show a mass uptake above ~250 °C, with a more activated regime above 450−500 °C, as already observed during exsolution of $BaFe_2(PO_4)_2$.[6,7] Above ~600 °C the observed plateau after the maximal uptake corresponds to full oxidation of Fe^{2+} to Fe^{3+}, as confirmed by Mössbauer spectroscopy (Table 2).

For the mixed Co/Fe compounds, the TGA mass uptake matches rather well ΔM_{calc} in the full y_{Co} range, though with slight discrepancies for $y_{Co} = 0.48$ and $y_{Co} = 1.32$ (Figure 5a). The Mössbauer spectra show only Fe^{3+} ions after heating (see Table 2). At this point, taking into account eqs 1 and 2Co, deviations of the TGA from ΔM_{calc} could denote deviations of the real Co/Fe ratio from the microprobe results, due to the averaging of several experimental points. For instance the 2.44% (for $y_{Co} = 0.48$) and 0.79% (for $y_{Co} = 1.32$) mass uptakes give ideal 0.62 and 1.56 stoichiometries, close to but different from those deduced from the analysis: i.e., 0.48 and 1.32.

Mössbauer spectra of the materials with different Fe/M ratios measured at 78 K are presented in Figure 6. Dealing with Mössbauer spectroscopy for Fe-rich compounds (y_{Co}= 0.48, 1.02) the $Fe^{3+}_{phase}/Fe^{3+}_{hematite}$ atomic ratio (~2) is in good agreement with eq 1. For these two samples, a broad distribution of nanometric size can be deduced from the proportion of Fe_2O_3 that undergoes the Morin transition at 78 K (see Table 2). The presence or absence of this spin-flip reorientation gives good indications about the nanosize of Fe_2O_3 clusters, as developed in ref 6. Because of intrinsic finite size effects related to lattice expansion, strains, defects, shape, etc., the Morin temperature of small Fe_2O_3 particles decreases with decreasing particle size and is suppressed to below 4 K for particles smaller than ~8−20 nm.[20,21]

For y_{Co}= 1.32, we find $Fe^{3+}_{phase}/Fe^{3+}_{hematite} \approx 3$ at 78 K, above the expected ratio of 2. In addition, no Morin transition was detected at 78 K, revealing nanosized domains. It is probable that, for such Co-rich composition, the iron diffusion paths are blocked by the more static Co^{2+} ions. At this point, the processes depicted by eqs 1 and 2Co could be in competition, as evidenced by TEM and EDX analyzes of the unwashed, depleted y_{Co} = 1.32 sample after TGA: the majority of the crystallites show a Fe/Co ratio close to 0.4/1.4, as expected after Fe exsolution to $BaFe^{3+}_{0.45}Co^{2+}_{1.3}(PO_4)_2$, with an increased concentration of Fe ions at their edges, as shown in Figure 7a. In contrast to our previous results on $BaFe_{1.33}(PO_4)_2$, we did not find clear evidence of Fe_2O_3 clusters by EDX, since Ba and P are found in the coating particles. This may be due to the size of the analyzed area such that the core is probed as well (the estimate EDX probe size is 20 nm). These results support the creation of highly intergrown nanosized Fe_2O_3 grains that are essentially superparamagnetic even at 78 K and so are not distinguished from the depleted phase by Mössbauer spectroscopy. This is in agreement with the Fe_2O_3 deficiency mentioned above. More rarely we found Co-rich particles

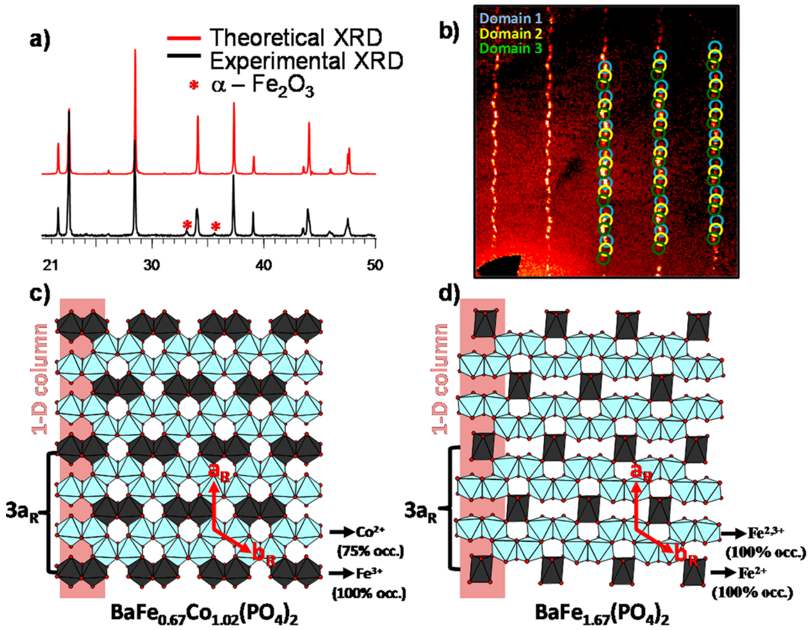

Figure 9. (a) Experimental and calculated powder XRD patterns for $BaFe_{0.67}Co_{1.02}(PO_4)_2$. (b) Precession image of the [*h* 0.33 *l*] layer in the rhombohedron with evidence of the three different twinned domains for $BaFe_{0.67}Co_{1.02}(PO_4)_2$ single crystal. Structural analogies between $BaFe_{0.67}Co_{1.02}(PO_4)_2$ (c) and $BaFe_{1.67}(PO_4)_2$ (d) with evidence of the $3a_R$ superperiod. The red arrows correspond to the parent rhombohedral cell.

coated by Co-rich nanograins with the absence of P and Ba (eq 2Co, assigned to Fe-doped Co_3O_4 clusters (Figure 7b). This shows a certain degree of inhomogeneity in the sample and demonstrates that, for very Co rich compositions, cobalt depletion via eq 2Co is possible. However, this phenomenon appears to be rare, taking into account the minor occurrence of such crystallites in our TEM analysis and our Co K edge XANES results.

For the $BaFe_{2-y}Ni_y(PO_4)_2$ solid solution (Figure 3b), significant discrepancies between TGA plots and ΔM_{calc} are observed for $y_{Ni} = 0.94$ and higher contents (see Figure 5b). At $y_{Ni} = 1.45$ the mass uptake turns into a mass loss above 450 °C. In addition to the possible deviation from the determinated stoichiometry from microprobe analysis, the dehydration of the $BaHPO_4$[22] secondary phase (see Microstructure), remaining in the sample after sonication, is responsible for this weight loss. It occurs according to the chemical reaction

$$2BaPO_4H \rightarrow Ba_2P_2O_7 + H_2O \qquad (3)$$

This was verified by PXRD analysis before and after thermal treatment (Figure 3b,d) showing the appearance of $Ba_2P_2O_7$ diffraction peaks after heating for the Ni-rich phase (see Figure3d). Concerning Mössbauer spectroscopy, the Fe_2O_3 content (~33%) matches perfectly the prediction of eq 1 for the Fe-rich compounds ($y_{Ni} = 0.46$), but for $y_{Ni} = 0.94$, an apparent deficiency of magnetically split Fe_2O_3 components is observed at 78 K (~28% instead of 33%). For $y = 1.45$ no magnetically ordered Fe_2O_3 is detected. However, these paramagnetic spectra could be fitted well by a model including Fe^{3+} doublet components with hyperfine parameters typical for superparamagnetic Fe_2O_3 (N15D1, N15D4 in Table 2). Because the latter parameters are close to those of Fe^{3+} in the main depleted phosphate phase and the corresponding doublets are completely overlapping, the exact amount of superparamagnetic Fe_2O_3 could not be unambiguously derived from these spectra. For that reason, its proportion was fixed as 1/3 during fitting. Again the high concentration of Ni^{2+} ions hamper Fe diffusion, in an even more drastic way. Here, the combined TEM/EDX analysis on heated $y_{Ni} = 1.45$, i.e. $BaFe_{0.37}Ni_{1.45}(PO_4)_2$, shows a homogeneous Fe:Ni ratio in the particles' core: e.g., 0.46:1.36 in Figure 8. In the external particles we find a diversity of behaviors from Fe enrichment to Fe exhaustion. Here, it is probable that the blocking Ni^{2+} ions can rearrange in the structure, leading to fragmentation of the crystals for Fe^{2+} removal and growth of Fe_2O_3 intergrown nanodomains under the given oxidation conditions. Again this leads to superparamagnetic behavior due to nanosizing of domains, in good agreement with Mössbauer spectroscopy.

$BaFe^{3+}{}_{0.67}Co^{2+}(PO_4)_2$ Crystal Structure and Possible Fe/Co Ordering. A single crystal with suitable size for XRD data collection was selected after heating $BaFe_{0.98}Co_{1.02}(PO_4)_2$ for 12 h at 600 °C. The crystal structure refinement was carried out to gain more insights about possible Fe−Co/V_{Fe} ordering in this sample, in relation to the discussion above. In a first approach, we processed a refinement in a rhombohedral cell corresponding to that of the parent of $BaM_2(XO_4)_2$ compounds. This preliminary refinement give clues about the metal stoichiometry, as reported for several $BaFe_{2-x}(PO_4)_2$ polytypes,[6] and led to the formula $Ba(Fe,Co)_{1.63}(PO_4)_2$ (a = 4.8096(14) Å, c = 23.6634(9) Å, space group $R\bar{3}$, R_{obs}= 3.66%, R_{all} = 3.76%) after refining the occupancy of the metal site 6c ($0,0,z \approx 1/3$). We note that the refined formula is very close to $BaM_{1.66}(PO_4)_2$, the ideal expected formula being $BaFe_{0.67}Co_1(PO_4)_2$ after Fe exsolution in $BaFe_1Co_1(PO_4)_2$ following eq 1. In this analysis there are no distinct cation sites for possible Fe/Co segregation.

In a second stage, taking into account weaker supercell reflections due to a partial order between metal and vacancies, it was possible to index the collected reflections fully on a triclinic unit cell (a = 8.3313(4) Å, b = 8.3316(4) Å, c = 8.3598(4) Å, α = 70.606(3)°, β = 99.558(3)°, γ = 120.013(3)°) given by the relation

Table 3. Atomic Distances and Associated Bond Valence Sum ($\sum s_{ij}$) Values, Calculated Using Parameters Associated to Fe^{3+} and Co^{2+} from Ref [28], of $BaFe_{0.67}Co(PO_4)_2$

	d (Å)
Ba1−O7	2.78(3) (×2)
Ba1−O12	2.82(4) (×2)
Ba2−O6	2.72(4)
Ba2−O6	2.83(4)
Ba2−O7	2.78(3)
Ba2−O12	2.79(4)
P1−O3	1.53(4)
P1−O5	1.62(2)
P1−O7	1.535(15)
P1−O10	1.49(3)
P2−O1	1.54(4)
P2−O4	1.61(2)
P2−O9	1.53(3)
P2−O12	1.518(18)
P3−O2	1.58(2)
P3−O6	1.534(19)
P3−O8	1.58(4)
P3−O11	1.50(3)
Co1−O1	2.14(3)
Co1−O2	2.02(2)
Co1−O2	2.03(3)
Co1−O3	2.16(3)
Co1−O9	2.09(4)
Co1−O10	2.10(2)
BVS: $2.05_{Co^{2+}}/2.47_{Fe^{3+}}$	
Co2−O1	2.26(3)
Co2−O3	2.11(2)
Co2−O4	2.08(3)
Co2−O5	2.05(2)
Co2−O11	2.08(3)
Co2−O11	2.05(2)
BVS: $1.99_{Co^{2+}}/2.39_{Fe^{3+}}$	
Fe1−O4	1.96(2)
Fe1−O5	2.00(3)
Fe1−O8	2.15(3)
Fe1−O8	2.09(2)
Fe1−O9	2.02(2)
Fe1−O10	2.10(3)
BVS: $2.79_{Fe^{3+}}/2.30_{Co^{2+}}$	

$$\begin{matrix} a_{\mathrm{Tricl}} \\ a_{\mathrm{Tricl}} \\ a_{\mathrm{Tricl}} \end{matrix} = \begin{bmatrix} -2 & -1 & 0 \\ 1 & -1 & 0 \\ 1/3 & -1/3 & 1/3 \end{bmatrix} \begin{matrix} a_{\mathrm{Rhombo}} \\ b_{\mathrm{Rhombo}} \\ c_{\mathrm{Rhombo}} \end{matrix}$$

As systematically found in all $BaFe_{2-x}(PO_4)_2$ phases reported so far (x = 2/7,1/2,2/3),[6,7] the collected crystal presents three twinning domains related by 120 and 240° around c^* due to the rhombohedral pseudosymmetry, as determined with the software CellNow.[23] In this case the superposition of the diffraction figures is particularly tricky, leading for instance to undulating lines of reflection spots in the $[h\ 0.33\ l]_{\mathrm{Rhombo}}$ precession images. These correspond to the superposition of three contributions, as shown in Figure 9b, and the full data set can be indexed using the three tilted domains. The crystal structure was solved and refined leading to final R_{obs}= 5.76%, with the three domain contributions equal to 0.365(10), 0.324(7), and 0.311(7). The occupancies of the three independent metal sites M1, M2, and M3 are refined to 91.2%, 69.0%, 72.5% but have been restrained to 100%, 75%, and 75% to match the ideal formula refined in the subcell.

For the honeycomb layer, the final structure is almost but not fully ordered in terms of M/V_M distribution due to full and 75% occupied distinct sites. M−O bond distances are given in Table 3. The layer shows ordering in 1D columns with a $3a_{\mathrm{Rhombo}}$ period. These columns are stacked to pave the 2D layers. It is striking that bond valence sums calculated in the Co^{2+} and Fe^{3+} hypotheses indicate possible chemical and charge segregation on the basis of bond valence sum calculations (BVS) (see Table 3). The M(2) and M(3) sites, which are 75% occupied, match well Co^{2+} ions, while the Fe^{3+} hypothesis is not relevant. In contrast, the occupancy of M(1) sites (100% occupied) by Fe^{3+} leads to more suitable BVS values. In addition a distribution with 100% Fe^{3+} in M1 and 75% Co^{2+} in M2 and M3 yields the ideal, charge-balanced formula $BaFe_{0.67}Co_1(PO_4)_2$ with respect to the site multiplicities. In addition, due to differences in ionic radii between high-spin Co^{2+} and high-spin Fe^{3+}, the good values and small dispersion of refined thermal parameters for all M and O sites play in favor of Fe/Co ordering. This is in good agreement with Mössbauer spectroscopy, as the Fe^{3+} component in the depleted $BaFe_{0.67}Co_1(PO_4)_2$ phase spectra is fitted by a single doublet with narrow line width, indicating a uniform surrounding for all the Fe^{3+} cations (Table 2). Although this hypothesis mostly relies on "empirical" BVS calculations, this full ordering remains highly plausible. To validate the refined model, we note that the calculated powder XRD diagram matches rather well the experimental powder pattern for the composition y_{Co} = 1.02 after thermal treatment (Figure 9a).

In the layers, the Co^{2+} sites (75% occupied) are arranged in zigzag chains running along the $\langle 210\rangle_{\mathrm{rhombo}}$ direction and are shown in blue in Figure 9c. The chains are linked together by the fully occupied Fe^{3+} dimers shown in gray. The analogy of this structure with that refined for $BaFe_{1.67}(PO_4)_2$ prepared after partial Fe exsolution is depicted in the Figure 9d. In the latter, the fully occupied Fe dimers are replaced by elongated $Fe^{2+}O_6$ octahedra, between Fe^{3+} chains. In $BaFe_{0.67}Co(PO_4)_2$ the segregation between Co^{2+} chains and Fe^{3+} sites demonstrates that not only Fe but also Co (and probably Ni) ions self-reorganize in the Fe-depleted layers. Further details about crystal data collection are reported in Table S-1 in the Supporting Information. Atomic coordinates and anisotropic displacements are shown in Table S-2 in the Supporting Information.

Magnetic Properties. Before exsolution, the $BaFe_{2-y}M_y(PO_4)_2$ (M = Co, Ni) compounds present potentially very complex mixed cation systems, as solid solutions among $BaCo_2(PO_4)_2$, a quasi 2D-XY helimagnet,[24] $BaNi_2(PO_4)_2$, a quasi 2D-XY antiferromagnet with collinear spins and a Kosterlitz−Thouless transition,[25] and $BaFe_2(PO_4)_2$, a 2D Ising ferromagnet.[4] The study of the magnetic properties of these solid solutions will be presented elsewhere.

After exsolution, $BaFe_{1.33}(PO_4)_2$ is antiferromagnetic with two sharp $\chi(T)$ anomalies at 16.2 and 4.2 K assigned to in-plane short-range ordering and 3D Néel-like antiferromagnetism across the ~8 Å interlayer spaces, respectively.[6] In general these are consistent with typical negative ~90° Fe^{3+}−O−Fe^{3+} superexchange couplings and similar exchanges can be

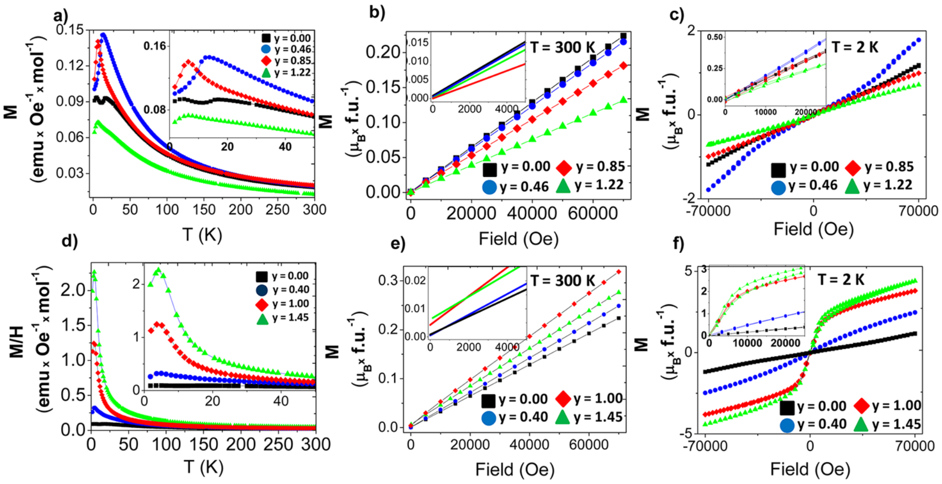

Figure 10. Magnetic characterization of $BaFe_{2-y}M_y(PO_4)_2$ after Fe exsolution: $\chi(T)$ for the mixed Fe/Ni (a) and Fe/Co (d) phases. Magnetization plots at 300 and 2 K for Fe/Ni (b, c) and Fe/Co (e, f) phases.

predicted for Fe^{3+}–O–Ni^{2+} and Fe^{3+}–O–Co^{2+} from Kanamori–Goodenough rules. After exsolution, we have considered the ideal formulas given in Table 1, predicted from the maximal exsolution of Fe^{2+} giving mixed Co^{2+}–Ni^{2+}/Fe^{3+} matrices (see eq 1). The samples have been washed from the Fe_2O_3 second phase by sonication, although a small fraction of the nanosized Fe_2O_3 cannot be fully removed.

The evolution of $\chi(T)$ for $Ba(Fe_{2-y}Ni_y)_{2-x}(PO_4)_2$ is shown in Figure 10a. Néel-like anomalies are evidenced at T_N = 13.7 K (y = 0.5, sharp), 6.6 K (y = 1, sharp), and 5.1 K (y = 1.5, broad), which show a progressive shift but remain located between the two peaks evidenced for y = 0. We note that, in any case, the transition temperatures are lower than T_N = 24 K reported for $BaNi_2(PO_4)_2$.[26] It most plausibly denotes an increasing distribution of short-range correlations due to metal vacancies in disordered Ni^{2+}/Fe^{3+} depleted lattices. The $M(H)$ magnetization plots confirm antiferromagnetic systems with no remanent moment or metamagnetic transition between 300 and 2 K (Figure10b,c), even though a smooth upturn is detected around H = 3 kOe for y_{Ni} = 0.5. In the paramagnetic regime, the values of effective moments were fitted between 5.70 and 7.58 μ_B, which roughly agrees with the values calculated from ideal formulas (, see Table 1). In addition to the spin–orbit coupling expected strong for Ni^{2+} ions, shifts from the theoretical values may denote partial removal of Fe_2O_3 and/or deviations from the ideal Fe/Ni stochiometries.

In the case of $Ba(Fe_{2-y}Co_y)_{1-x}(PO_4)_2$, magnetic plots in Figure 10 show that the situation is more complicated. The $M(H)$ plots at room temperature for $BaFe_{0.65}Co_{1.02}(PO_4)_2$ and $BaFe_{0.45}Co_{1.32}(PO_4)_2$ show a weak remanent moment (Figure10d). This is most probably related to the intimate coating of nanotextured Fe_2O_3 grains at the crystallite surface, leading to superparamagnetism with blocking temperatures above room temperature. For these two compositions the concave shapes of $\chi(T)$ plots have been fitted using $\chi = C/(T - \Theta) + \chi_0$, using the approximation of a constant superparamagnetic magnetization. This same approximation was successfully applied to $BaFe_{2-x}(PO_4)_2$.[7] The fits are very good (see Figure S-1 in the Supporting Information), giving χ_0 = 0.021 and 0.020 emu mol^{-1} Oe^{-1} for $BaFe_{0.65}Co_{1.02}(PO_4)_2$ and $BaFe_{0.45}Co_{1.32}(PO_4)_2$, respectively, and show positive Curie–Weiss temperatures which may be due to the superparamagnetic impurity. In these two samples, disordered Co^{2+}-rich domains are expected, reminiscent of the $BaCo_2(XO_4)_2$ phases (X = P^{5+}, As^{5+}) which show in-plane helical magnetic structures, easy spin alignment under magnetic field, and magnetization steps at low temperature for the arsenate.[27] Therefore, it is not surprising that in $BaFe_{0.65}Co_{1.02}(PO_4)_2$ and $BaFe_{0.45}Co_{1.32}(PO_4)_2$ the $M(H)$ plot at 2 K shows an abrupt step in the low-field region below μ_0H = 0.6 T, above which it recovers the $M(H)$ slope typical of the Fe-rich compounds. The susceptibility measured for $BaFe_{0.45}Co_{1.32}(PO_4)_2$ is very large; it reaches ~2 emu mol^{-1} Oe^{-1}, which is very similar to values reported for $\chi_{a,b}$ in $BaCo_2(PO_4)_2$.[27] We conclude that in the two deficient systems the magnetic behavior is driven by antiferromagnetic Fe^{3+}–O–Fe^{3+}, Fe^{3+}–O–M^{2+}, and M^{2+}–O–M^{2+} through edge-shared octahedra. For Ni-rich compounds, under an applied field the antiferromagnetism (AFM) is much more robust than that in Co-rich compounds, in good agreement with the parent Ni (AFM with site to site collinear spins) and Co compounds (soft helical AFM with nearly FM chains).

■ CONCLUSION

The oxidation of mixed-metal $Ba(Fe,M)^{2+}{}_2(PO_4)_2$ (M = Co, Ni) phases after heating in air at 600 °C for 12 h leads to Fe-deficient phases with a full oxidation of Fe^{2+} to Fe^{3+} and preserving divalent M cations. The exsolved iron ions form nanoclusters at the surface of the parent phase, with an strong dependence of the cluster size on the Fe/M ratio. In the oxidation of the parent $BaFe^{2+}{}_2(PO_4)_2$ phase, the reorganization of Fe ions and V_{Fe} vacancies after exsolution inside the 2D layers leads to a variety of supercell orderings with period related to the Fe-depletion rate. In the mixed-metal systems, although M^{2+} ions hamper the Fe diffusion, the distribution of Fe^{3+} and M^{2+} centers is almost fully ordered, which proves that not only Fe ions but also Co^{2+}/Ni^{2+} ions are mobile in this crystal structure. This easy reorganization proves that the metal diffusion paths are confined within the 2D layers. This opens broad possibilities to achieve new metal-depleted layered topologies, by tuning the initial Fe/M ratio and also the oxidation conditions for partial iron oxidation. Taking into account our experimental observation for the possible (but low) exsolution of cobalt in cobalt-rich phases, attempts for a significant exsolution of cobalt in $BaCo_2(PO_4)_2$ and $BaNi_2(PO_4)_2$ under strongly oxidizing conditions, such as high-pressure oxygen, are currently under investigation.

■ ASSOCIATED CONTENT

Ⓢ Supporting Information

The Supporting Information is available free of charge on the ACS Publications website at DOI: 10.1021/acs.inorgchem.5b01360.

> Single-crystal collection data, atomic coordinates and displacements of $BaFe_{0.67}Co(PO_4)_2$, and Curie−Weiss fit for $BaFe_{2-y}M_y(PO_4)_2$ (PDF)
>
> Crystallographic data (CIF)

■ AUTHOR INFORMATION

Corresponding Author

*E-mail for O.M.: olivier.mentre@ensc-lille.fr.

Present Address

$^{\perp}$Université Lille Nord de France, UCCS, UMR-CNRS 8181, ENSCL-USTL, Villeneuve d'Ascq, France.

Notes

The authors declare no competing financial interest.

■ ACKNOWLEDGMENTS

R.D. thanks ENS Lyon for financial support. This work was carried out under the framework of the MAD-BLAST project supported by the ANR (Grant ANR-09-BLAN-0187-01). The Fonds Européen de Développement Régional (FEDER), CNRS, Région Nord Pas-de-Calais, and Ministère de l'Education Nationale de l'Enseignement Supérieur et de la Recherche are acknowledged for funding of X-ray diffractometers. The TEM facility in Lille, France, is supported by the Conseil Regional du Nord-Pas de Calais and the European Regional Development Fund (ERDF). The authors also thank the 11-BM beamline staff and Dr. Pascal Roussel for helpful discussions. Use of the Advanced Photon Source at Argonne National Laboratory was supported by the U.S. Department of Energy, Office of Science, Office of Basic Energy Sciences, under Contract No. DE-AC02-06CH11357.

■ REFERENCES

(1) Regnault, L. P.; Burlet, P.; Rossatmignod, J. *Physica B+C* **1977**, *86-88*, 660−662.

(2) Rogado, N.; Huang, Q.; Lynn, J. W.; Ramirez, A. P.; Huse, D.; Cava, R. J. *Phys. Rev. B* **2002**, *65*, 144443.

(3) Heinrich, M.; von Nidda, H. K.; Loidl, A.; Rogado, N.; Cava, R. J. *Phys. Rev. Lett.* **2003**, *91*, 054422.

(4) Kabbour, H.; David, R.; Pautrat, A.; Koo, H. J.; Whangbo, M. H.; Andre, G.; Mentre, O. *Angew. Chem., Int. Ed.* **2012**, *51*, 11745−11749.

(5) David, R.; Pautrat, A.; Filimonov, D.; Kabbour, H.; Vezin, H.; Whangbo, M. H.; Mentre, O. *J. Am. Chem. Soc.* **2013**, *135*, 13023−13029.

(6) Blazquez Alcover, I.; David, R.; Daviero-Minaud, S.; Filimonob, D.; Huvé, M.; Roussel, P.; Kabbour, H.; Mentré, O. *Cryst. Growth Des.*, Accepted for publication, 2015.

(7) David, R.; Kabbour, H.; Filimonov, D.; Huve, M.; Pautrat, A.; Mentre, O. *Angew. Chem., Int. Ed.* **2014**, *53*, 13365−13370.

(8) Eymond, S.; Martin, C.; Durif, A. *Mater. Res. Bull.* **1969**, *4*, 595−599.

(9) David, R.; Kabbour, H.; Pautrat, A.; Mentre, O. *Inorg. Chem.* **2013**, *52*, 8732−8737.

(10) Rodriguez-Carvajal, J. *Fullprof*; 2001; http://www.ill.eu/sites/fullprof/.

(11) *SAINT+*; Bruker Analytical X-ray Systems, Madison, WI, 2001 (x2).

(12) *SADABS, Bruker/Siemens Area detector absorption and other corrections*; Bruker Analytical X-ray Systems: Madison, WI, 2011 (x2).

(13) Palatinus, L.; Chapuis, G. *J. Appl. Crystallogr.* **2007**, *40*, 786−790.

(14) Petricek, V.; Palatinus, L. *JANA 2000*; 2005.

(15) Shannon, R. D. *Acta Crystallogr., Sect. A: Cryst. Phys., Diffr., Theor. Gen. Crystallogr.* **1976**, *32*, 751−767.

(16) Kondoh, S.; Kitamura, M.; Morimoto, N. *Am. Mineral.* **1985**, *70*, 737−746.

(17) Hamelet, S.; Gibot, P.; Casas-Cabanas, M.; Bonnin, D.; Grey, C. P.; Cabana, J.; Leriche, J. B.; Rodriguez-Carvajal, J.; Courty, M.; Levasseur, S.; Carlach, P.; van Thournout, M.; Tarascon, J. M.; Masquelier, C. *J. Mater. Chem.* **2009**, *19*, 3979−3991.

(18) Muraliganth, T.; Manthiram, A. *J. Phys. Chem. C* **2010**, *114*, 15530−15540.

(19) Amisse, R.; Hamelet, S.; Hanzel, D.; Courty, M.; Dominko, R.; Masquelier, C. *J. Electrochem. Soc.* **2013**, *160*, A1446−A1450.

(20) Bodker, F.; Hansen, M. F.; Koch, C. B.; Lefmann, K.; Morup, S. *Phys. Rev. B: Condens. Matter Mater. Phys.* **2000**, *61*, 6826−6838.

(21) Lu, H. M.; Meng, X. K. *J. Phys. Chem. C* **2010**, *114*, 21291−21295.

(22) Hebbar, K. C.; Dharmaprakash, S. M.; Rao, P. M. *Bull. Mater. Sci.* **1991**, *14*, 1219−1223.

(23) Sheldrick, G. M. *CELL NOW, program for unit cell determination*; http://shelx.uni-ac.gwdg.de/SHELX.

(24) Regnault, L.; Rossat-Mignod, J.; Villain, J.; De Combarie, A. *J. Phys. Colloques* **1978**, *39*, C6-759−C6-761.

(25) Regnault, L. P.; Rossatmignod, J.; Henry, J. Y.; Dejongh, L. J. *J. Magn. Magn. Mater.* **1983**, *31−34*, 1205−1206.

(26) Regnault, L. P.; Henry, J. Y.; Rossatmignod, J.; Decombarieu, A. *J. Magn. Magn. Mater.* **1980**, *15−18*, 1021−1022.

(27) Jongh, L. J. D. *Magnetic Properties of Layered Transition Metal Compounds*; Kluwer Academic: Dordrecht, The Netherlands, 1990.

(28) Brese, N. E.; O'Keeffe, M. *Acta Crystallogr., Sect. B: Struct. Sci.* **1991**, *47*, 192−197.